



Nanoscale

Galvanic Replacement of Intermetallic Nanocrystals as a Route Toward Complex Heterostructures

Journal:	<i>Nanoscale</i>
Manuscript ID	NR-ART-11-2020-008255.R1
Article Type:	Paper
Date Submitted by the Author:	18-Jan-2021
Complete List of Authors:	Chen, Alexander; Indiana University - Bloomington, Chemistry Endres, Emma; Indiana University Bloomington Ashberry, Hannah; Indiana University - Bloomington, Chemistry Bueno, Sandra; Indiana University - Bloomington, Chemistry Chen, Yifan; Indiana University - Bloomington, Chemistry; Nanjing Normal University Skrabalak, Sara; Indiana University - Bloomington, Chemistry

SCHOLARONE™
Manuscripts

ARTICLE

Galvanic Replacement of Intermetallic Nanocrystals as a Route Toward Complex Heterostructures

Received 00th January 20xx,
Accepted 00th January 20xx

Alexander N. Chen,^a Emma J. Endres,^a Hannah M. Ashberry,^a Sandra L. A. Bueno,^a Yifan Chen^a and Sara E. Skrabalak^{*a}

DOI: 10.1039/x0xx00000x

Galvanic replacement reactions are a reliable method for transforming monometallic nanotemplates into bimetallic products with complex nanoscale architectures. When replacing bimetallic nanotemplates, even more complex multimetallic products can be made, with final nanocrystal shapes and architectures depending on multiple processes, including Ostwald ripening and the Kirkendall effect. Galvanic replacement, therefore, is a promising tool in increasing the architectural complexity of multimetallic templates, especially if we can identify and control the relevant processes in a given system and apply them more broadly. Here, we study the transformation of intermetallic PdCu nanoparticles in the presence of HAuCl₄ and H₂PtCl₆, both of which are capable of oxidizing both Pd and Cu. Replacement products consistently lost Cu more quickly than Pd, preserved the crystal structure of the original intermetallic template, and grew a new phase on the sacrificial template. In this way, atomic and nanometer-scale architectures are integrated within individual nanocrystals. Product morphologies included faceting of the original spherical particles as well as formation of core@shell and Janus-style particles. These variations are rationalized in terms of differing diffusion behaviors. Overall, galvanic replacement of multimetallic templates is shown to be a route toward increasingly exotic particle architectures with control exerted on both Angstrom and nanometer-scale features, while inviting further consideration of template and oxidant choices.

1. Introduction

The chemical and physical properties of a multimetallic nanocrystal, and therefore its utility, depend strongly upon the internal organization of its constituent atoms, that is, its architecture.^{1,2} Architecture-dependent properties of nanocrystals can be seen at two length scales. First, the atomic-scale organization of atoms within a single phase controls the chemical and physical properties of the phase itself. Atomic-scale organization can manifest as different crystal structures possessing the same stoichiometry, such as ordered intermetallic compared with disordered random alloy phases. Intermetallic phases display long-range atomic ordering of the elements, while random alloy phases do not.³ Second, the nanometer-scale organization of different phases in a nanocrystal can lead to synergistic or antagonistic relationships between juxtaposed phases. Two notable nanoscale architectures include core@shell particles and Janus particles. The ability to select architectures at both of these length scales is important in determining a nanocrystal's properties. For example, intermetallic nanocrystals can display greater durability than their random alloy analogs due to low diffusion rates and high bond energies, and also frequently increase

catalytic activity and selectivity due to their atomic ordering at surfaces.^{1,4} Meanwhile, core@shell and Janus particles can have strong communication between their component phases, such as when a core strains shell atoms to tune their surface chemistry or when the plasmonic side of a Janus particle produces hot carriers to drive catalytic activity in an adjacent phase.⁵⁻⁹ Architectural control is, therefore, crucial for designing nanocrystals to fit a desired set of properties.

Few synthetic tools are generalizable to the point that they can easily integrate architectures across both atomic and nanometer length scales. The galvanic replacement reaction, whereby a metal salt with a high reduction potential is reduced by a metallic sacrificial template with a lower reduction potential, is one route to reliably producing multimetallic nanocrystals with complex architectures. Typical galvanic replacement reactions are conducted on monometallic templates, yielding bimetallic alloy or heterostructure particles, depending on the redox pair involved.¹⁰⁻¹³ The high predictability of galvanic replacement with monometallic templates makes it a good candidate for increasing architectural complexity in more complex templates.

^a Department of Chemistry, Indiana University - Bloomington, Bloomington, Indiana 47405, United States.

Electronic Supplementary Information (ESI) available: methods and materials, additional TEM, STEM, EDS, XRD and XPS data, and additional discussion of topics introduced in the main text. See DOI: 10.1039/x0xx00000x

Studies of bimetallic sacrificial templates are less common, but the choices of sacrificial template and oxidant strongly influence the final product in the literature. We recently studied galvanic replacement of AgPd heterodimers by Au salts and found that the less noble metal should be replaced most quickly, and that vacancy diffusion occurs anisotropically during such a reaction.¹⁴ However, it is reasonable to expect that atoms in a pure monometallic phase of a heterodimer would behave differently from those in a multimetallic phase. Indeed, Cobley and co-workers showed that HAuCl₄ could successfully dealloy AgPd alloyed nanoboxes, but Na₂PdCl₄ could not dealloy AgAu nanoboxes, despite being able to galvanically replace pure Ag.¹⁵ Also, Li and co-workers showed that intermetallic and random alloy AuCu₃ templates behaved differently when galvanically replaced by HAuCl₄. Mainly, there are different energy barriers for interdiffusion, where the slow diffusion in the intermetallic lattice inhibited the Kirkendall effect and led to slower Cu leaching than for the random alloy.¹⁶ Thus, the literature suggests that the galvanic replacement of intermetallic templates by a salt that can oxidize both elements comprising the template would yield great architectural complexity, but the way in which replacement will proceed must still be determined. Gaining such knowledge is central for applying the noted strengths of galvanic replacement to the synthesis of complex nanocrystals with control of both atomic and nanoscale architecture.

Here, we galvanically replace intermetallic PdCu (B2) and random alloy PdCu (A1) sacrificial nanoparticle templates with HAuCl₄ and H₂PtCl₆. Both AuCl₄⁻ ($E_{\text{red}} = 0.93$ V vs. the standard hydrogen electrode, SHE) and PtCl₆²⁻ ($E_{\text{red}} = 0.68$ V vs. SHE; PtCl₄²⁻/PtCl₆²⁻ $E_{\text{red}} = 0.76$ V vs. SHE) are thermodynamically capable of oxidizing Pd to PdCl₄²⁻ ($E_{\text{red}} = 0.59$ V vs. SHE), Cu to Cu⁺ ($E_{\text{red}} = 0.52$ V vs. SHE), Cu to Cu²⁺ ($E_{\text{red}} = 0.34$ V vs. SHE), or Cu⁺ to Cu²⁺ ($E_{\text{red}} = 0.15$ V vs. SHE).¹⁷ The resulting nanostructures consist of an intermetallic or alloy PdCu domain with an undisturbed superlattice for the B2 PdCu case, and a Pd-rich exterior upon which Au or Pt domains grow. Cu is selectively oxidized before Pd, and is found in solution as both Cu⁺ and

Cu²⁺. Cu⁺ may in turn serve as a reducing agent for Au and Pt species in solution or at the surfaces of other particles.

2. Results and Discussion

2.1. Morphological and architectural evolution

To begin, monodisperse, hydrophobic, oleylamine-capped intermetallic B2 PdCu nanoparticle templates (Figure S1, 9.9 ± 0.8 nm diameter) were synthesized according to a modified literature procedure.¹⁸ These hydrophobic nanoparticles were transferred to an aqueous hexadecyltrimethylammonium bromide (CTAB) solution following another literature procedure¹⁹ in order to take advantage of the well-documented aqueous reduction potentials listed above. Galvanic replacement reactions consisted of slow injection (0.25 mL / min using a syringe pump) of aqueous 0.1 mM HAuCl₄ into the aqueous solution of PdCu nanoparticles. Figure 1 shows representative transmission electron microscopy (TEM) images of particles at various stages in the replacement reaction, with low-magnification TEM images in Figures S2, S3 and S4 showing a larger number of particles from the samples shown in Figure 1, to better judge monodispersity. The initial nanoparticles are single-phase spheroids (Figure S1) and eventually become two-phase Janus heterodimers after addition of 15 mL HAuCl₄ (Figure 1C, TEM). Both domains of the heterodimers appear more faceted than the original nanoparticles. Intermediate points, such as in Figure 1B, show polydisperse products, with heterodimers being mixed with core@shell structures of varying shell roughness and relatively faceted spheroids. Early points, such as in Figure 1A, show spheroidal nanoparticles.

Scanning transmission electron microscopy coupled with energy-dispersive X-ray spectroscopy (STEM-EDS) provides elemental maps of the nanocrystal types at the three points just mentioned in Figure 1 and bring to light differing diffusion behaviors for Cu, Pd, and Au. The early stage (Figure 1A) spheroidal product has a low Au signal that is strongest away from the center of the particle, indicating a core@shell structure with a possibly discontinuous or alloyed shell (see

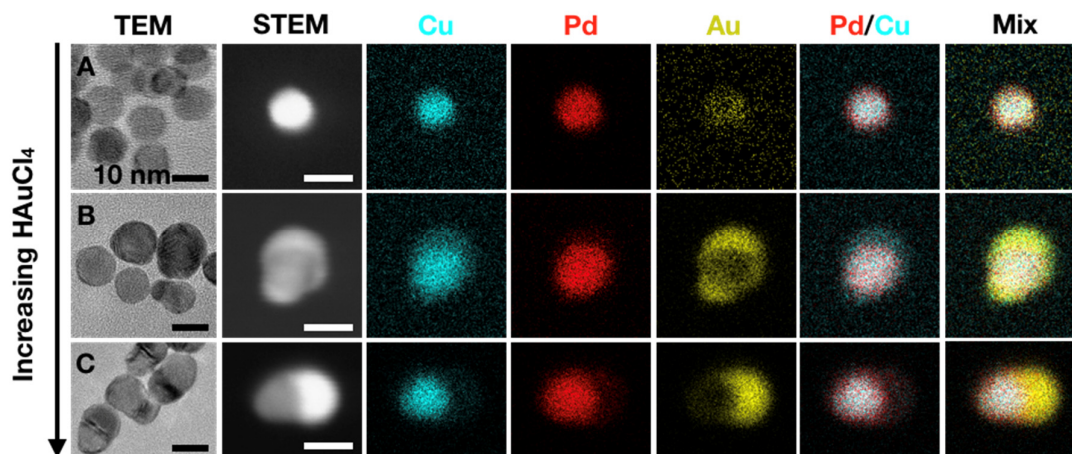


Figure 1. TEM images, STEM images and EDS maps of galvanic replacement products as (row A) 6, (B) 9 and (C) 15 mL 0.1 mM HAuCl₄ are added to intermetallic PdCu seeds. Cyan, Cu; red, Pd; yellow, Au. All scale bars are 10 nm.

Figure S5 for line scans). Overlaying only the Pd and Cu signals also reveals that the exterior is Pd-rich. In the intermediate stage (Figure 1B), a Au phase of variable thickness surrounds the PdCu domain, corresponding to the rough shell seen in TEM. As was noted previously, this sample is polydisperse in that it includes morphologies seen at all stages of the reaction. The sample shown in Figure 1B was deemed representative of the intermediate stage because it has a common morphology seen by low-magnification TEM in Figure S3, and this morphology disappears completely in the late stage, implying that many particles pass through this intermediate morphology. All previously noted morphologies as well as variations on the intermediate represented by Figure 1B are seen when using slightly more or less HAuCl_4 (Figure S6), further supporting that the morphology examined in Figure 1B represents an intermediate stage. Interestingly, the PdCu domain in Figure 1B, which still contains strong Pd and Cu signals, is surrounded by a weaker Cu signal that approximately follows the Au signal. Cu outside of the PdCu phase suggests that metallic Cu diffuses outwards separately from being oxidized, while Pd does not seem to diffuse elsewhere. Outward Cu diffusion during galvanic replacement has been attributed to the Kirkendall effect before but was observed in AuCu_3 random alloy templates,^{16,20,21} and specifically not in intermetallic templates, where energy barriers for interdiffusion were deemed too high.¹⁶ That Cu diffusion would occur in the B2 PdCu template indicates that the high energy barrier for diffusion was overcome here. Unlike typical instances of the Kirkendall effect where nanoparticles develop hollows and the oxidant metal diffuses inward to make an alloy,²⁰⁻²³ the apparently absent or very slow interdiffusion of Pd and Au here means that no voids or Pd-Au mixing are visible.

In the late stage (Figure 1C), the Au shell has transformed into a single spheroidal phase attached to one side of the PdCu phase. This transition from a relatively isotropic shell to a disjointed shell, and then to a heterodimer indicates that

diffusion of Au on the PdCu surface, presumably to reach a thermodynamically more favorable configuration, is relatively easy. The late stage Pd signal is also visibly much stronger than the Cu signal, hinting at selective oxidation of Cu. In addition, the Cu-rich exterior has disappeared, leaving a PdCu phase with a Pd-rich exterior once more, suggesting that diffusing Cu is oxidized quickly as it approaches the nanocrystal surface. Lastly, it is clear that from beginning to end, the particles' Au content increases.

Figure 1 showed the overall diffusion behaviors of Cu, Pd, and Au, while hinting at compositional changes. High-resolution STEM in Figure 2 provides more precise phase information, with a closer look at a PdCu-Au Janus particle. Figure 2A clearly shows two major phases on either side of a PdCu-Au interface. One phase has a superlattice of alternating columns of atoms with different z-contrasts, that is, the intermetallic crystal lattice. A closer look at the edges of the intermetallic phase shows multiple layers with far less contrast between neighboring columns, agreeing with the observation in Figure 1A and Figure 1C of a Pd-rich exterior. Looking at the interface itself, we can see an epitaxial relationship between PdCu and Au, with a calculated lattice mismatch of 3.7% (Figure S7, see SI for full discussion). The observed segregation of Au at a PdCu{100} plane in particular can be attributed to this relatively low lattice mismatch. Even so, segregation into a single, larger phase suggests that the B2 PdCu-Au interfacial free energy is high enough to disfavor large interfaces, and, as Figure 1 pointed out, Au diffuses readily enough to allow for easy segregation. Significant Au surface diffusion has been observed from beam-induced heating by *in situ* TEM, or heating at 200 °C in vacuum,²⁴⁻²⁶ which could be comparable to heating from the refluxing aqueous solution here. There is also some overlap between the two phases visible at the interface, resulting in an intermediary Pd-rich phase: an elemental map and accompanying line scan in Figure 2B show that the interface is rich in Pd, with almost no Cu present when the Au signal rises

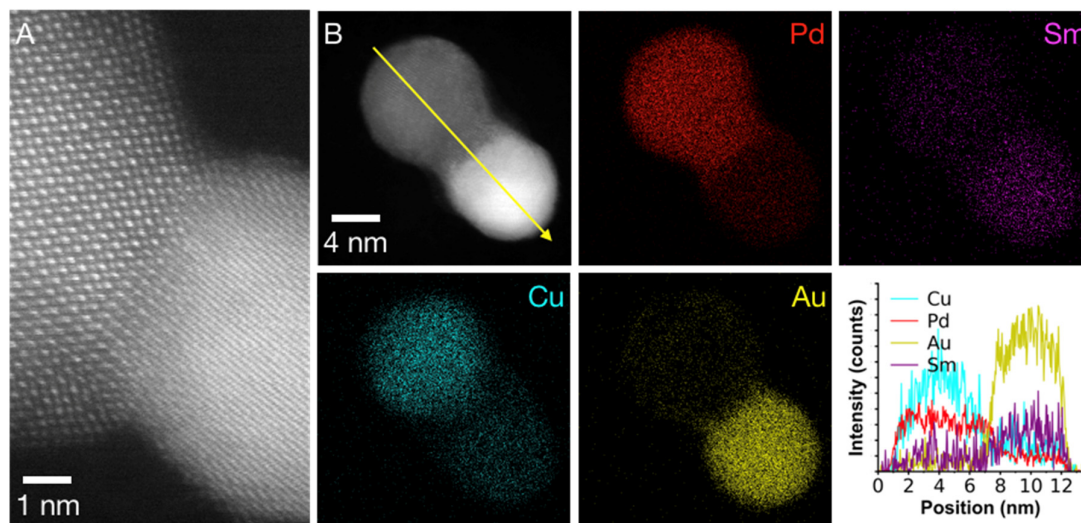


Figure 2. (A) High-resolution STEM image of the middle of a galvanic replacement product from adding 15mL 0.1mM HAuCl_4 to intermetallic PdCu seeds, and (B) high-resolution STEM-EDS elemental map of a different particle from the same sample, with corresponding line scan down the yellow arrow. Cyan, Cu; red, Pd; yellow, Au; purple, Sm.

above the Sm signal chosen to represent the background. Pd diffusion toward the interface may be driven by energetically more favorable interactions between B2 PdCu and a Au-Pd alloy (3.7% calculated lattice mismatch for pure Au) than between B2 PdCu and pure Pd (8.7% calculated lattice mismatch).

2.2. Bulk analyses

To accompany the above microscopic analysis, bulk elemental compositions as a function of HAuCl_4 added were determined using EDS on large areas in a scanning electron microscope (SEM-EDS). The resulting elemental compositions are plotted in Figure 3, with atomic percentages of Cu, Pd, and

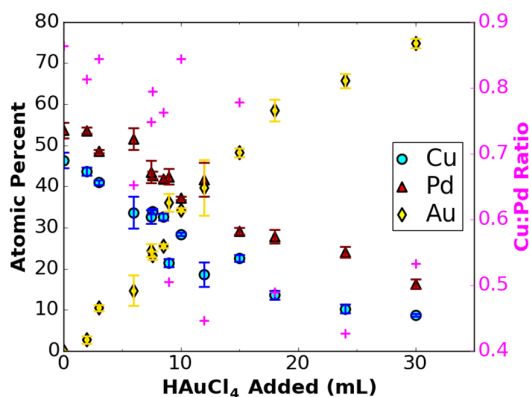


Figure 3. Evolving atomic percentages of Cu, Pd and Au in intermetallic PdCu templates as 0.1 mM HAuCl_4 is added to them, as determined by energy dispersive X-ray spectroscopy. Error bars represent standard deviations.

Au as a function of the volume of 0.1 mM HAuCl_4 added. These atomic percentages show first that Au content increases approximately linearly with volume of titrant, suggesting that HAuCl_4 behaves in approximately the same manner for the duration of the reaction. Second, Cu and Pd contents both decrease, but at different rates: the Cu:Pd ratio begins at 0.86 but decreases as more HAuCl_4 is added, ending at 0.53. Such a large change in the Cu:Pd ratio shows that Cu is selectively oxidized from the B2 PdCu templates more quickly than Pd, agreeing with the single-particle analysis in Figure 1. A closer look at Figure 3 shows that while the Cu:Pd ratio decreases overall, it does increase at some points. These irregular changes should be attributed to increased sample polydispersity at intermediate stages of reaction (see SI and Figure S8 for full discussion).

Figure 2 showed that the B2 phase is preserved on at least some particles; however, the diminishing Cu:Pd ratio in Figure 3 raises the question of to what extent the B2 phase persists as the Cu:Pd ratio moves beyond what the phase diagram should allow.²⁷ X-ray diffraction (XRD) revealed that the lattice was preserved in the sample as a whole, and across many different volumes of titrant added. Specifically, Figure 4 displays the characteristic 30.2° superlattice peak of B2 PdCu in XRD patterns of many galvanic replacement products over the course of the reaction. From the unmodified templates with 0 mL 0.1 mM HAuCl_4 added to at least 10 mL, the superlattice peak remains unambiguously present, even as Au peaks grow in

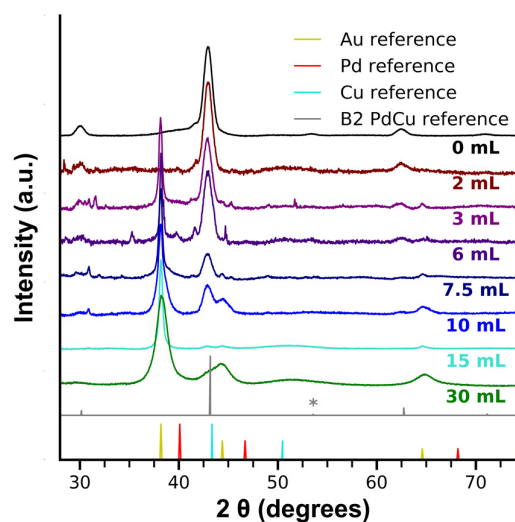


Figure 4. Background-subtracted XRD patterns corresponding to products obtained when B2 PdCu templates are galvanically replaced by various volumes of 0.1 mM HAuCl_4 . The asterisk marks a low-intensity B2 reference peak.

intensity. At 15 mL, the superlattice peak is not visible; however, the intensities of most peaks are muted aside from the Au{111} peak, likely due to preferred particle orientations. The most intense PdCu peak is still present even at 30 mL, where the superlattice peak is again not visible. Rietveld refinement of the 30 mL XRD pattern, in Figure S9, indicates that the sample composition at this very late stage is 27% B2 PdCu and 73% Au, further confirming that the crystal structure of the shrinking PdCu phase is preserved throughout the galvanic replacement reaction. So, to reconcile the decreasing Cu:Pd ratio with this steady preservation of the B2 phase, we refer back to the discussion of Figure 2, where we noted the Pd-rich exterior of the B2 phase as well as Pd diffusion toward the PdCu-Au interface. The absence of a distinct Pd peak in Figure 4 suggests that a strained Au-Pd alloy may be forming at the interface as the B2 phase shrinks and leaves behind excess Pd that diffuses toward either the exterior or the Au phase.

2.3. Effect of injection rate

Previous sections demonstrated that diffusion and redox reactions both contribute to the final product's shape and architecture. The literature has shown that changing the relative rates of competing processes involved in nanoparticle syntheses can strongly affect morphology and architecture by favoring various kinetic or thermodynamic products.²⁸⁻³⁰ Here, we investigate kinetic insights gained from changing the relative rates of diffusion and redox reactions. Up to this point, all galvanic replacement reactions were performed using constant injection rates and concentrations of titrant solution. We therefore attempted to increase the rate of the redox reaction by increasing the injection rate.

Figure S10 shows the effects of increasing injection rate and injection volume when adding 0.1 mM HAuCl_4 to B2 PdCu templates. A diagonal trend is seen, where increasing the injection rate produces a similar effect on particle morphology

as increasing the injection volume. Briefly, low injection rate and low volume produced spheroids, while higher injection rate or injection volume produced Janus-type heterostructures (See SI for full discussion). However, it is difficult to attribute this trend to increased rate of galvanic exchange, as injected solutions were at room temperature while the reaction solution was refluxing. Temperature drops from quick injection likely lead to burst nucleation, similarly to hot injection reactions,³¹ which complicates any assertion concerning the effect of changing the redox reaction's rate. Even so, these results show two routes toward heterodimers.

An extreme case of quick injection revealed a kinetically important step in the reaction: a smaller volume of excess HAuCl_4 (720 μL 10 mM) was used with the intent to drive the reaction to completion, yielding large products rich in planar defects (Figure S11, see SI for full discussion). The products were much larger than the original PdCu templates. Given that Cu and Pd are the only available species that can reduce HAuCl_4 , this suggests that several B2 seeds would need to be oxidized to account for such large products. This can be explained through either Ostwald ripening,^{16,32} or oxidized Cu passing through intermediate oxidation states. To investigate oxidation states of soluble metal ions, X-ray photoelectron spectra (XPS) were taken of a dried supernatant obtained from centrifuging a reaction solution after adding 3 mL 0.1 mM HAuCl_4 . Notably, the Cu 2p region of the spectrum in Figure S12 has a large Cu 2p_{3/2} peak at 932.1 eV and a smaller one at 935.1 eV, which are close to literature values for CuCl (932.0 eV)³³ and CuCl₂ (934.7 eV),³⁴ respectively. The presence of Cu⁺ species in solution is significant at this early stage in the galvanic replacement reaction, as it means that there are species capable of reducing Au ions in solution, without needing metallic Pd or Cu. The presence of Cu²⁺ ions is also significant, as it implies that Cu⁺ does get oxidized to Cu²⁺. Thus, Au³⁺ could be reduced to sparingly soluble Au⁺ species without deposition by metallic Pd or Cu, making particles shrink, while all Au ions can be reduced by Cu⁺ elsewhere to grow a larger particle than a single PdCu template should be able to account for.

2.4. Intermetallic vs. random alloy

In addition to studying replacement of intermetallic B2 PdCu nanoparticles (Figure S1, 9.9 \pm 0.8 nm diameter), random alloy A1 PdCu (Figure S13, 9.9 \pm 1.0 nm diameter) spheroids of approximately the same size were synthesized³⁵ and treated to similar experiments. These studies were undertaken to identify the similarities and differences in behavior between the two crystal structures. Bulk EDS in Figure 5 shows a much more constant decrease in Cu:Pd ratio as HAuCl_4 is added than in Figure 3: as before, Cu is oxidized more quickly than Pd. XRD analysis in Figure S14 shows that the PdCu alloy phase shrinks while moving away from the pure Cu reference and toward the pure Pd reference, while a Au-rich phase grows. The shift in XRD peak position indicates that lattice constant changes are occurring, unlike the intermetallic case (Figure 4). This difference in lattice constant evolution can be attributed to the greater stability¹⁸ and lower diffusion rates inside intermetallic phases.¹⁶ Morphological evolution in Figure S15 shows some

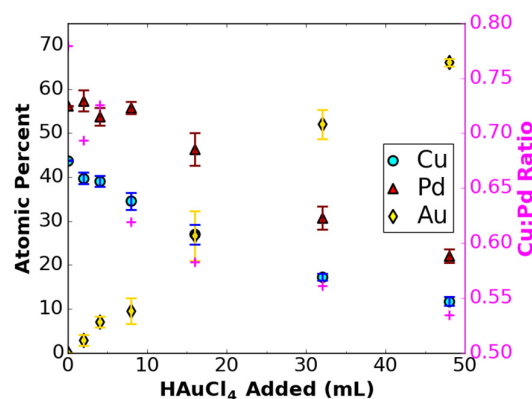


Figure 5. Evolving atomic percentages of Cu, Pd and Au in random alloy PdCu templates as 0.1 mM HAuCl_4 is added to them, as determined by energy dispersive X-ray spectroscopy. Error bars represent standard deviations.

similarity to the intermetallic results. Random alloy templates become relatively faceted, and grow spheroidal domains on their surfaces (Figure S15A-C). However, as larger amounts of HAuCl_4 are added, dumbbell-like structures disappear in favor of spheroids (Figure S15D-F). Less phase segregation in the late-stage product is unsurprising, as A1 PdCu possesses the same crystal structure as Au, allowing for better miscibility. Thus, while the redox reactions follow the same trend, there are significant differences in the phase segregation behavior as Au deposits on the intermetallic and random alloy templates.

Studies of sample polydispersity reveal similarities to B2 templates in that multiple morphologies are present in some samples, despite not being visible by SEM-EDS (Figure S16, see SI for full discussion). The polydispersity of both A1 and B2 replacement products hints at the significance of nucleation kinetics in this galvanic replacement process. Figure S17 maps the elemental composition of a cluster of A1 templates that have undergone varying degrees of replacement. Specifically, a particle with virtually no Au, one with a Au shell and one with Au spheroids growing at the surface all sit in the captured cluster. The Au shell and Au spheroids recall different stages identified for intermetallic templates, while the apparently unreacted particle is either at a much earlier stage than the other two, or has been oxidized without any deposition. Coexistence of so many different types of particles indicates that this galvanic replacement reaction is quick to deposit Au on some templates, and slow on others. The large difference in Au deposition rates for different particles supports the separation of redox reactions from heterogeneous nucleation of Au for both A1 and B2 seeds.

2.5. HAuCl_4 vs. H_2PtCl_6

The results obtained with the oxidant HAuCl_4 highlight predictable redox behavior coupled with less predictable deposition and diffusion behavior. To gain better insight into the generality of results obtained using HAuCl_4 , H_2PtCl_6 was also studied as an oxidant with B2 PdCu templates. Bulk-scale composition and phase analysis show behavior similar to HAuCl_4 . When slowly injecting aqueous solutions of 0.2 mM

H_2PtCl_6 at a rate of 0.25 mL/min into suspensions of intermetallic PdCu seeds, EDS analysis in Figure S18 shows that Cu is once again oxidized more quickly than Pd. XRD patterns in Figure S19 show a shrinking intermetallic PdCu phase alongside a growing phase composed of some mixture of Pd and Pt, where Pd and Pt are difficult to differentiate by XRD due to their very similar lattice constants.

Two notable differences arise when comparing the particle morphologies obtained by injecting H_2PtCl_6 instead of HAuCl_4 . First, no Janus particles were observed. Instead, Figure S20 shows TEM images of faceted convex products over a wide range of volumes of H_2PtCl_6 added, with no additional phase obviously visible by z-contrast. A tilt study in Figure S21 confirms that many of the particles are octahedra. High-resolution STEM and elemental mapping in Figure 6 clarify the mode of Pt deposition; the convex particles are composed of intermetallic PdCu cores and random alloy PdPt shells. The line scan in Figure 6 supports interdiffusion of Pt and Pd near the surface, though not of Pt into PdCu. Pd and Pt mix more readily than Pd and Au, which is reasonable given the very small calculated lattice mismatch of 0.9%. Concerning the lack of Janus particles: conformal Pt shells are known to form on Pd seeds in conditions of slow deposition.^{36,37} The literature showed that galvanic

observed in the present work. Given the clear diffusion shown by Au in earlier sections, the current section suggests that Pt has much lower surface mobility. It is possible that segregated Pt domains could form with a greatly extended reaction time, but longer reaction times would likely also involve much more Pt deposition.

A second difference between H_2PtCl_6 and HAuCl_4 is that significant populations of very small particles can be found in some samples, as seen most clearly in Figure S20C. Elemental mapping in Figure S22 reveals that the very small particles are composed of a mixture of Pd and Pt, with the Cu signal being comparable to the Sm signal used to represent the background. Given that Pd^{2+} ($E_{\text{red}} = 0.59$ V) and Pt^{4+} ($\text{PtCl}_6^{2-}/\text{PtCl}_4^{2-}$ $E_{\text{red}} = 0.68$ V; $\text{PtCl}_4^{2-}/\text{Pt}$ $E_{\text{red}} = 0.76$ V) are both capable of being reduced by Cu (Cu^+/Cu $E_{\text{red}} = 0.52$ V; $\text{Cu}^{2+}/\text{Cu}^+$ $E_{\text{red}} = 0.15$ V),¹⁷ the small particles likely result from homogeneous nucleation of Pd and Pt in solution, perhaps reduced by Cu^+ . XPS analysis of a supernatant from an early-stage product in Figure S23 confirms that Cu^+ can also be found in solution when H_2PtCl_6 is the oxidant. Homogeneous nucleation here has some precedent as growth of Pt on Pd seeds has been reported to proceed by homogeneous nucleation of Pt in solution, followed by oriented attachment.³⁸ Overall, this comparison of HAuCl_4 and H_2PtCl_6 as

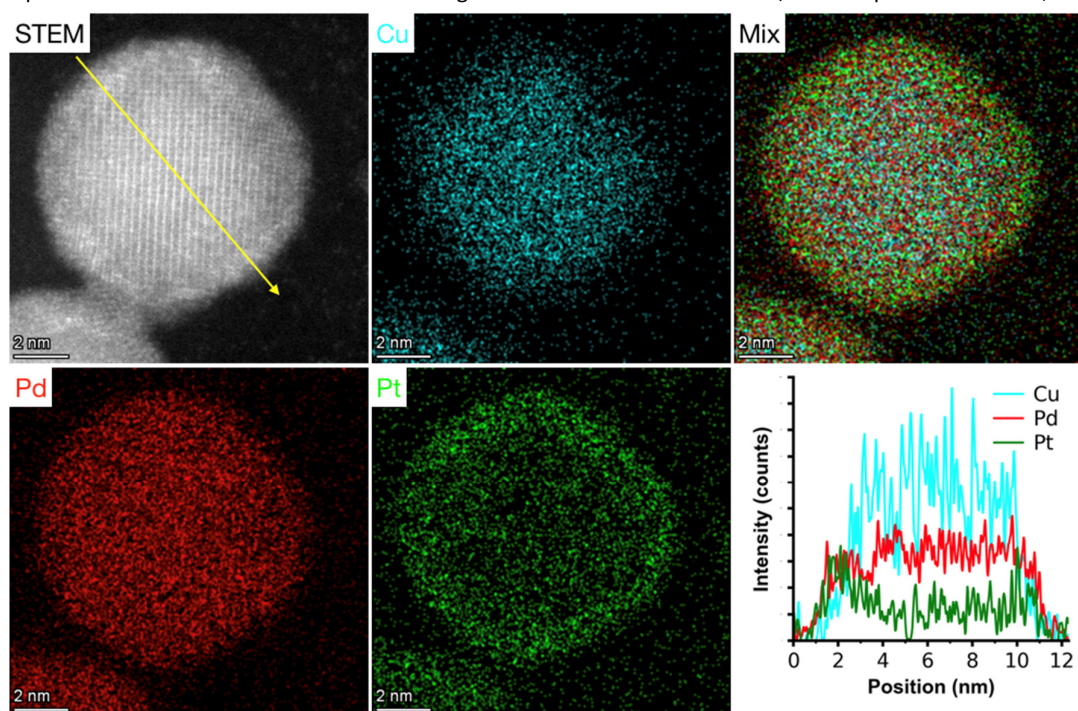


Figure 6. High-resolution STEM image of a galvanic replacement product from adding 6 mL 0.2mM H_2PtCl_6 to intermetallic PdCu seeds, and corresponding high-resolution STEM-EDS elemental map, with a line scan down the yellow arrow. Cyan, Cu; red, Pd; green, Pt.

replacement of sharp Pd nanocubes by H_2PtCl_6 produced truncated cubic shapes upon heating at 90 °C for 0.5 h post-injection, likely corresponding to a thin shell as in the present work, but also more and corner-directed Pt deposition upon heating for 4–20 h post-injection.¹² The difference in amounts of deposition between 0.5 and 20 h indicates a very slow reduction of PtCl_6^{2-} , at least by Pd, which agrees with the conformal shells

oxidants for the galvanic replacement of B2 PdCu suggests that intermetallic templates paired with various oxidants should expect similar trends such as selective oxidation and crystal structure preservation, while also expecting differences based on surface mobility, intermediate oxidation states, and nucleation and growth modes.

3. Conclusions

The present work has shown both similarities and differences between three pairs of bimetallic PdCu sacrificial templates and metal ion oxidants. To summarize, in every case, Cu was oxidized more quickly than Pd and the sacrificial template's phase was preserved while providing growth sites for a different phase of deposited material. Faceting was seen for all products, though more with H₂PtCl₆ than HAuCl₄, implying facet-selective etching, facet-selective deposition, or both. Intermetallic PdCu templates rigidly preserved the intermetallic lattice while excess Pd either remained near the surface or diffused toward the depositing material. Random alloy PdCu templates preserved an alloyed phase whose lattice constant shifted to accommodate selective Cu oxidation. Au, likely due to high surface mobility, formed segregated domains on PdCu templates, more for B2 than for A1 PdCu. Pt, presumably due to lower surface mobility, formed conformal shells, but also saw competition between homogeneous and heterogeneous nucleation.

In revealing similarities between A1 and B2 PdCu, and between HAuCl₄ and H₂PtCl₆, we show that galvanic replacement is a useful tool for increasing the nanoscale architectural complexity of sacrificial templates already possessing either Angstrom-scale or nanometer-scale architectural complexity along predictable lines. Predictable features include selective oxidation and, for ordered intermetallics, preservation of the template phase. In revealing differences, we show that there are more variables than the classic example of replacing monometallic Ag by HAuCl₄ might suggest, including crystal structures, diffusion, reduction and oxidation kinetics. We note that these currently less predictable elements are centered around nanoscale features such as morphology. Overall, this study increases our understanding of galvanic replacement for multimetallic templates and the synthetic levers that can influence it in a reaction involving multiple species to reduce and to oxidize, toward the ultimate goal of achieving the desired architecturally complex multimetallic product.

Conflicts of interest

There are no conflicts to declare.

Acknowledgements

This work was supported by the US National Science Foundation (NSF CHE 1904499). S.L.A.B. thanks NSF DGE 1342962 for a Graduate Research Fellowship. Y.C. thanks the China Scholarship Council (Grant No. 201806860028) for financial support. E.J.E. was supported by the 2019 Summer Research Internship Program sponsored by IU's Women in STEM Living-Learning Center. All authors also acknowledge support from Indiana University, and thank Dr. Changqiang Chen in the Materials Research Laboratory Central Research Facilities at the University of Illinois at Urbana-Champaign for conducting atomic resolution STEM and EDS, and Indiana University's

Electron Microscopy Center, Nanoscale Characterization Facility and Molecular Structure Center for access to instrumentation.

References

- J. T. L. Gamler, H. M. Ashberry, S. E. Skrabalak and K. M. Koczkur, *Adv. Mater.*, 2018, **30**, 1801563.
- N. E. Motl, A. F. Smith, C. J. DeSantis and S. E. Skrabalak, *Chem. Soc. Rev.*, 2014, **43**, 3823-3834.
- D. Wang and Y. Li, *Adv. Mater.*, 2011, **23**, 1044-1060.
- Y. Yan, J. S. Du, K. D. Gilroy, D. Yang, Y. Xia and H. Zhang, *Adv. Mater.*, 2017, **29**, 1605997.
- M. Kim, M. Lin, J. Son, H. Xu and J.-M. Nam, *Adv. Opt. Mater.*, 2017, **5**, 1700004.
- J. L. Brooks, C. L. Warkentin, D. Saha, E. L. Keller and R. R. Frontiera, *Nanophotonics*, 2018, **7**, 1697-1724.
- D. F. Swearer, H. Zhao, L. Zhou, C. Zhang, H. Robotjazi, J. M. Martirez, C. M. Krauter, S. Yazdi, M. J. McClain, E. Ringe, E. A. Carter, P. Nordlander and N. J. Halas, *Proc. Natl. Acad. Sci. U. S. A.*, 2016, **113**, 8916-8920.
- J. T. L. Gamler, H. M. Ashberry, X. Sang, R. R. Unocic and S. E. Skrabalak, *ACS Appl. Nano Mater.*, 2019, **2**, 4538-4546.
- J. T. L. Gamler, A. Leonard, X. Sang, K. M. Koczkur, R. R. Unocic, M. Engel and S. E. Skrabalak, *Nanoscale Adv.*, 2020, **2**, 1105-1114.
- S. E. Skrabalak, L. Au, X. Li and Y. Xia, *Nat. Protoc.*, 2007, **2**, 2182-2190.
- P. H. C. Camargo, Y. Xiong, L. Ji, J. M. Zuo and Y. Xia, *J. Am. Chem. Soc.*, 2007, **129**, 15452-15453.
- H. Zhang, M. Jin, J. Wang, W. Li, P. H. Camargo, M. J. Kim, D. Yang, Z. Xie and Y. Xia, *J. Am. Chem. Soc.*, 2011, **133**, 6078-6089.
- X. Xia, Y. Wang, A. Ruditskiy and Y. Xia, *Adv. Mater.*, 2013, **25**, 6313-6333.
- A. N. Chen, S. M. McClain, S. D. House, J. C. Yang and S. E. Skrabalak, *Chem. Mater.*, 2019, **31**, 1344-1351.
- C. M. Cobley, D. J. Campbell and Y. Xia, *Adv. Mater.*, 2008, **20**, 748-752.
- G. G. Li, M. Sun, E. Villarreal, S. Pandey, S. R. Phillpot and H. Wang, *Langmuir*, 2018, **34**, 4340-4350.
- P. Vanýsek, in *CRC Handbook of Chemistry and Physics*, ed. J. R. Rumble, CRC Press/Taylor & Francis, Boca Raton, FL, 99 edn.
- C. Wang, X. Sang, J. T. L. Gamler, D. P. Chen, R. R. Unocic and S. E. Skrabalak, *Nano Lett.*, 2017, **17**, 5526-5532.
- L. Wu, J. Yu, L. Chen, D. Yang, S. Zhang, L. Han, M. Ban, L. He, Y. Xu and Q. Zhang, *J. Mater. Chem. C*, 2017, **5**, 3065-3071.
- S. Thota, S. Chen and J. Zhao, *Chem. Commun.*, 2016, **52**, 5593-5596.
- S. Thota, Y. Zhou, S. Chen, S. Zou and J. Zhao, *Nanoscale*, 2017, **9**, 6128-6135.
- L. Au, X. Lu and Y. Xia, *Adv. Mater.*, 2008, **20**, 2517-2522.
- E. González, J. Arbiol and V. F. Puntes, *Science*, 2011, **334**, 1377-1380.
- D. J. Smith, A. K. Petford-Long, L. R. Wallenberg and J. O. Bovin, *Science*, 1986, **233**, 872-875.
- A. Surrey, D. Pohl, L. Schultz and B. Rellinghaus, *Nano Lett.*, 2012, **12**, 6071-6077.
- W. Albrecht, E. Bladt, H. Vanrompay, J. D. Smith, S. E. Skrabalak and S. Bals, *ACS Nano*, 2019, **13**, 6522-6530.

27. P. R. Subramanian and D. E. Laughlin, *J. Phase Equilib.*, 1991, **12**, 231-243.
28. X. Xia, S. Xie, M. Liu, H. C. Peng, N. Lu, J. Wang, M. J. Kim and Y. Xia, *Proc. Natl. Acad. Sci. U. S. A.*, 2013, **110**, 6669-6673.
29. Y. Xia, X. Xia and H.-C. Peng, *J. Am. Chem. Soc.*, 2015, **137**, 7947-7966.
30. Y. Yang, J. Liu, Z. W. Fu and D. Qin, *J. Am. Chem. Soc.*, 2014, **136**, 8153-8156.
31. C. de Mello Donega, P. Liljeroth and D. Vanmaekelbergh, *Small*, 2005, **1**, 1152-1162.
32. D. Alloyeau, G. Prévot, Y. Le Bouar, T. Oikawa, C. Langlois, A. Loiseau and C. Ricolleau, *Phys. Rev. Lett.*, 2010, **105**, 255901.
33. R. P. Vasquez, *Surf. Sci. Spectra*, 1993, **2**, 138-143.
34. R. P. Vasquez, *Surf. Sci. Spectra*, 1993, **2**, 160-164.
35. J. T. L. Gamler, A. Leonardi, H. M. Ashberry, N. N. Daanen, Y. Losovyj, R. R. Unocic, M. Engel and S. E. Skrabalak, *ACS Nano*, 2019, **13**, 4008-4017.
36. X. Wang, S. I. Choi, L. T. Roling, M. Luo, C. Ma, L. Zhang, M. Chi, J. Liu, Z. Xie, J. A. Herron, M. Mavrikakis and Y. Xia, *Nat. Commun.*, 2015, **6**, 7594.
37. H. Zhang, M. Jin, J. Wang, M. J. Kim, D. Yang and Y. Xia, *J. Am. Chem. Soc.*, 2011, **133**, 10422-10425.
38. B. Lim, M. Jiang, T. Yu, P. H. C. Camargo and Y. Xia, *Nano Res.*, 2010, **3**, 69-80.